

Interleaved dual-species arrays of single atoms using a passive optical element and one trapping laser

Chengyu Fang¹, Jared Miles³, Jonathan Goldwin³, Martin Lichtman³, Matthew Gillette³,
Michael Bergdolt³, Sanket Deshpande¹, Sam A. Norrell², Preston Huft²,
Mikhail A. Kats^{*1,2}, and Mark Saffman^{2,3}

¹Department of Electrical and Computer Engineering, University of Wisconsin-Madison,
1415 Engineering Drive, Madison, WI, 53706, USA

²Department of Physics, University of Wisconsin-Madison, 1150 University Avenue,
Madison, WI, 53706, USA

³Infleqtion, Inc., Madison, WI, 53703, USA

Abstract

We demonstrate trapping of individual rubidium (Rb) and cesium (Cs) atoms in an interleaved array of bright tweezers and dark bottle-beam traps, using a microfabricated optical element illuminated by a single laser beam. This trapping approach is simple and robust compared to common approaches that use active optoelectronic components and multiple laser wavelengths, and can be easily adapted for other atomic species.

1 Introduction

Arrays of trapped neutral atoms are being rapidly developed for quantum sensing, communication, and computing applications[1]. Scaling up to large numbers of trapped atoms in well-ordered arrays is necessary for large-scale computation and other quantum-information applications. Large arrays have been achieved using sophisticated optical systems comprising high-power lasers and active beam-shaping components such as acousto-optic deflectors (AODs) [2], spatial light modulators (SLMs) [3, 4], and digital mirror devices (DMDs) [5, 6]. New developments utilize interleaved arrays of two different atomic species for error correction and noise reduction[7, 8, 9, 10] where, for example, one type of atom can be a computation qubit and the other a measurement qubit. Trapping multiple species of atoms simultaneously adds to system complexity, especially when using multiple trapping lasers with different wavelengths and active electro-optical components [8]. System complexity can

*Corresponding author: mkats@wisc.edu

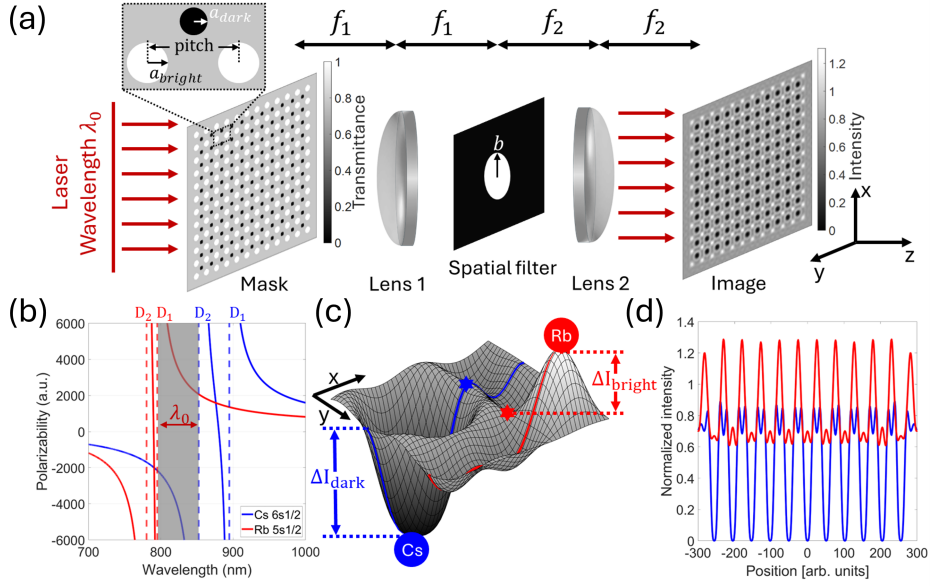


Figure 1: Working principle of the dual-species array generator. **(a)** Schematic of the $4f$ system to produce an interleaved array of bright and dark traps. A laser at λ_0 illuminates the optical mask, followed by a $4f$ system with a spatial filter, to produce the trapping light at the back focal plane of lens 2. A spatial filter with radius b is placed between lens 1 and lens 2 to filter out high-frequency components to produce a Gaussian-like trapping profile. **(b)** The wavelength of the input beam λ_0 should be selected between the Rb D1 line and Cs D2 line, such that the polarizability of one species is positive and the other negative. **(c)** Calculated intensity contour (vs. position) for one period in the image plane, showing one bright trap for Rb and one dark trap for Cs. The intensity difference ΔI between the trap centers and the locations identified by blue and red stars represent the intensity depths. **(d)** The intensity line profiles of dark traps (blue line) and bright traps (red line), as identified in Fig. 1(c). The dark traps and the bright traps are optimized to achieve zero intensity and maximum intensity, respectively, at the trap centers, using a shared spatial filter.

be reduced by using specially fabricated passive components to generate arrays of optical traps[11, 12, 13, 14, 15].

Here, we demonstrate a simple, all-passive optical system that can transform a single high-power laser beam into an array of interleaved dark (blue-detuned) and bright (red-detuned) traps, with each type of trap exclusively hosting a certain species of atom [Fig. 1(a, b)]. This system is enabled by a passive optical intensity mask which can be inexpensively fabricated with conventional scalable microelectronics processes (photolithography, thin-film evaporation, liftoff, and wet etching), and generates three levels of transmittance (zero, medium, high) while managing the phase between the different regions, which forms the traps. The mask is highly robust, functioning over a wide range of laser wavelengths with substantial tolerance to fabrication errors. Using this technique with a single 825 nm laser, we experimentally demonstrated interleaved single-atom arrays of ^{87}Rb in bright traps and ^{133}Cs in dark traps, each with a loading rate close to 50%.

2 Working principle and design

Our approach, shown in Fig. 1(a), is to send a laser beam with single wavelength λ_0 through a mask with three transmittance levels: fully transmitting regions to form bright traps, fully opaque regions to form the dark traps, and an intermediate background level to provide an intensity contrast for both type of traps. This mask creates a bright flat-top beam array interleaved with a dark “flat-bottom” beam array. The beams comprising both arrays are then shaped into Gaussian-like profiles via spatial filtering [11]. To make the size of the traps suitable for single-atom trapping, the beams are de-magnified and relayed to the atom trapping region using a sequence of lenses in the optical system.

To enable simultaneous two-species trapping of ^{87}Rb and ^{133}Cs at different sites with a single laser, we select a laser wavelength λ_0 between the Rb D1 line (795 nm) and the Cs D2 line (852 nm), such that the dynamic polarizabilities of Rb and Cs have opposite signs [Fig. 1(b)]. In this scheme, a region of high intensity is attractive to Rb atoms, but repulsive to Cs atoms, and vice versa. We note that there are additional windows of opposing polarizabilities in the $\sim 780 - 790$ nm and $\sim 880 - 895$ nm ranges, however these regions fall near atomic resonances, resulting in high scattering rate and significantly mismatched polarizabilities, potentially causing unequal trap depths between the two species.

To form the appropriate potential gradients, the intensity distribution of flat-top and flat-bottom beams generated with the mask must be smoothed to generate Gaussian-like trapping profiles, which can be accomplished by Fourier-plane spatial filtering with an iris at the intermediate plane of a $4f$ imaging system [11]. Smoothing the intensity at the Fourier plane rather than directly on the mask avoids design and fabrication complications, such as the use of grayscale fabrication. Since the dark traps and the bright traps are adjacent to each other, interference between them can result in features that deviate from the desired trapping pattern in the image plane. Fig. 1(c) shows the calculated intensity contour of one unit cell in the image plane, for a design that will be described later in this paper. With the selected trapping wavelength λ_0 , Rb atoms are trapped in the bright traps and Cs atoms are trapped in the dark traps. The intensity line profiles of dark and bright traps, shown in Fig. 1(d), demonstrate the trapping profiles are both Gaussian-like. Note that we previously used a similar approach to create a large single-species array of Cs atoms in blue-detuned dark traps [11].

To achieve the best intensity profiles at the image plane for atom trapping, the following requirements should be approached: (a) To maximize the depth of the bright traps, the bright traps should have maximum intensity at the trap sites for a given input power; (b) To maximize the depth of the dark traps, the dark traps should have zero intensity at the trap-site centers; (c) To maximize the energy efficiency of the system, the trapping depth should be equal for the bright and the dark traps for the two atomic species, otherwise more power is required to compensate for the weaker traps.

In our $4f$ imaging system, the spatial filter is placed at the back focal plane of the first lens (i.e., in the Fourier plane). The amplitude distribution at the filter plane is the Fourier transform of the amplitude distribution at the mask (flat-top beams for bright traps, and flat-bottom beams for dark

traps). The spatial filter is used to remove the high-frequency components to make the trapping profile at the image plane Gaussian-like, which localizes the atoms at the centers of the traps. To achieve the best quality of the traps, certain conditions need to be satisfied, especially the size relationships between the radius of the apertures a_{bright} , the radius of the opaque disks a_{dark} , and the iris radius b [Fig. 1(a)].

In the case of bright traps, the beam-amplitude profile after the first lens with focal lens f_1 becomes a Fourier transform of the flat-top beam, which is $J_1(r)/r$, i.e., an airy disk ($J_1(r)$ is the first-order Bessel function of the first kind, and r is the radial distance from the center of each disk). To maximize the depth of the bright traps with a single aperture, the iris radius needs to block the light past the radius where the amplitude goes from positive to zero for the first time, which is shown in Eq. (1)

$$b = \frac{f_1}{ka_{\text{bright}}} r_1^{(1)}, \quad (1)$$

where k is the wavenumber of the trapping laser, f_1 is the focal length of the first lens, and $r_1^{(1)}$ is the first zero of the first-order Bessel function. This condition ensures that the beam-amplitude profile in the image plane after f_2 , A_{bright} , is maximized.

Similarly, in the case of dark traps, the amplitude profile at the image plane is the input amplitude A_0 minus the complementary Gaussian-like beam profile A_{dark} . The calculation is similar to bright traps but with a key difference: instead of maximizing the center amplitude for bright traps, the center amplitude of dark traps needs to be zero, which means $A_0 - A_{\text{dark}}(r = 0) = 0$. Since $A_{\text{dark}}(r = 0)$ is larger than A_0 given the condition in Eq. (1), more light needs to be filtered at the Fourier plane to reduce the amplitude of the complementary flat-top beam down to A_0 . To achieve this, the size requirement between the dark disk radius a_{dark} and b is shown in Eq. (2) below, where $r_1^{(0)}$ is the first zero of the zeroth-order Bessel function

$$b = \frac{f}{ka_{\text{dark}}} r_1^{(0)}. \quad (2)$$

As discussed previously, both bright and dark traps share a single iris in the Fourier plane. Thus the iris radii in eqs. (1) and (2) are equal, which gives the necessary relationship between the dark and bright trap radii:

$$\begin{aligned} \frac{f}{ka_{\text{dark}}} r_1^{(0)} &= \frac{f}{ka_{\text{bright}}} r_1^{(1)} \\ \Rightarrow a_{\text{bright}} &= \frac{r_1^{(1)}}{r_1^{(0)}} a_{\text{dark}} \approx 1.6 a_{\text{dark}} \end{aligned} \quad (3)$$

The arrangement and spacing of the traps depends on the application. As an example, for Rydberg atom-based quantum computing [16], atoms are typically spaced at $3 - 10 \mu\text{m}$ on a square grid, while the traps for single atoms need to have a waist of $\sim 1 \mu\text{m}$. An appropriate choice is to make the period

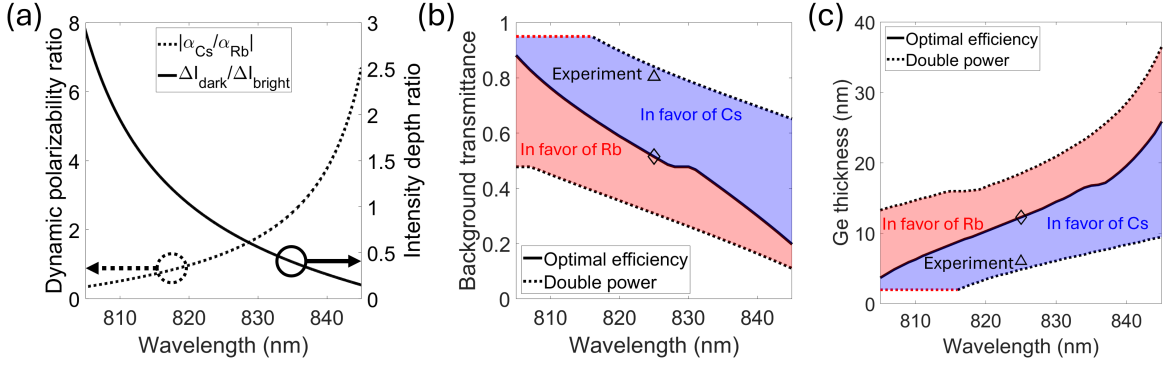


Figure 2: Design of the mask background transmittance. **(a)** The ground-state dynamic polarizability ratio between Cs and Rb, $|\alpha_{\text{Cs}}/\alpha_{\text{Rb}}|$, decreases as a function of wavelength. To achieve equal trapping depths, we need an intensity-depth ratio, $\Delta I_{\text{dark}}/\Delta I_{\text{bright}}$, which is the reciprocal of the polarizability ratio. **(b, c)** The needed (b) background transmittance and (c) the Ge thickness as a function of wavelength, showing the optimal design (solid line), which has equal trapping depth between Cs and Rb, and a range of less-efficient designs (colored regions). The dashed lines indicate designs that require double the incident power compared to the optimum design, to achieve the same trapping depth for the weaker trap. In the blue region, the trapping profile favors Cs atoms (in the dark traps) due to higher-than-optimal background transmittance. Similarly, in the red region, the trapping profile is in favor of Rb atoms (in the bright traps) due to lower-than-optimal background transmittance. Note that when the transmittance is very high (i.e., Ge thickness is very thin), the interference ripples (shown in Fig. 1(c)) start to be comparable to the bright traps. Due to this, we set a cap of the transmittance at 95% and a bottom of the Ge thickness at 2 nm to avoid the bright-trap intensity depth being smaller than the interference ripples. The triangles mark the experimentally demonstrated design. The diamonds mark the optimal design for a trap laser of wavelength 825 nm.

about 4 times larger than the size of the apertures for this application. Other arrangements such as hexagonal clusters[17], Kagome lattices[18], and triangular lattices[19] have been used for quantum simulation and computation demonstrations. These and other patterns can be readily achieved by using different arrangements of the bright and dark disks on the mask.

To achieve the third requirement – equal trapping depth for both species atoms – the intensity depths for dark and bright traps need to satisfy eq. (4)

$$\alpha_{\text{dark}}\Delta I_{\text{dark}} = \alpha_{\text{bright}}\Delta I_{\text{bright}}, \quad (4)$$

where α is the ground-state polarizability of the atoms (shown in Fig. 1(b)) and ΔI is the intensity depth of the traps (shown in Fig. 1(c)). This requirement helps the mask to create effective dark and bright traps with the lowest input laser power. To control the intensity depths, we use a semi-transparent background layer to provide contrast for both bright and dark traps. If a longer wavelength is used, the required intensity depth ratio between dark and bright traps decreases, decreasing the required background transmittance, as shown in Fig. 2(b).

Notably, our approach is robust to errors in the background transmittance. When the background transmittance is not optimal, both species of atoms can still be trapped, but at a cost of higher laser

power to compensate for the weaker traps. For example, if we are willing to double the minimum required power, a range of background transmittance can be accepted, which is shown in Fig. 2(b). Higher background transmittance favors the dark traps (here, Cs atoms), while lower background transmittance favors the bright traps (here, Rb atoms).

3 Materials and non-ideal phases

On the intensity mask, there are regions with three different levels of transmittance T (shown in Fig. 3(a)): (1) transparent regions ($T_{\text{bright}} = 1$) for generating the bright traps; (2) a background ($0 < T_{\text{background}} < 1$); and (3) an opaque region ($T_{\text{background}} = 0$) for generating dark traps. Additionally, an important requirement is that there is no substantial phase difference between the background and the bright regions, which creates additional constraints on how the background region should be designed.

To make the highly transparent regions, we used a window substrate with anti-reflection (AR) coatings on both sides. For the opaque regions, we deposited 100 nm of gold, which results in a transmittance less than 0.1%.

To achieve the desired transmittance in the background region, we used a thin layer of material with an intermediate degree of absorption such that (a) a subwavelength-thick layer can result in enough absorption of the incident light without a significant phase shift, and (b) the absorption is not so high, such that the transmittance can be controlled on the single-percent level by changing deposition conditions such as deposition time. We found that amorphous semiconductors with band gaps smaller than the photon energy, such as amorphous germanium (a-Ge), can work in this role. Here, we chose electron-beam evaporated Ge, which can be smooth for thin layers [20]. We used the transfer-matrix method (TMM) to calculate the transmittance and phase shift in the background region coated with a-Ge, and the results are shown in Fig. 3(b, c).

Based on the calculated transmittance and phase profiles, we performed a simulation consisting of a Fourier transform of the electric field after the mask to yield the field distribution in the Fourier plane, spatial filtering at the Fourier plane, then an inverse Fourier transform to find the field distribution at the image plane. This simulation considers interference between the dark and bright traps, which enables us to precisely calculate what a-Ge thickness is required to achieve the desired transmittance to satisfy Eq. (4), shown in Fig. 2(c). When the background material thickness is not optimal, this mask can still be used to trap both species of atoms, but requires using a higher laser power.

In our design, using a 825 nm laser, ^{87}Rb atoms are trapped in the bright traps and ^{133}Cs atoms are trapped in the dark traps. The ground-state dynamic polarizability ratio of Cs and Rb is about 2 for the design wavelength $\lambda_0 = 825$ nm, so the intensity depth ratio of dark and bright traps is around 0.5 (in Fig. 2(a)). Assuming that we can accept doubling the optimal laser power, a Ge thickness from 5 nm to 18 nm can trap both species of atoms.

We evaporated an a-Ge layer, with thickness of approximately 6 nm, to form the background region, which according to our TMM calculation has a transmittance of 0.8 for $\lambda = 825$ nm and

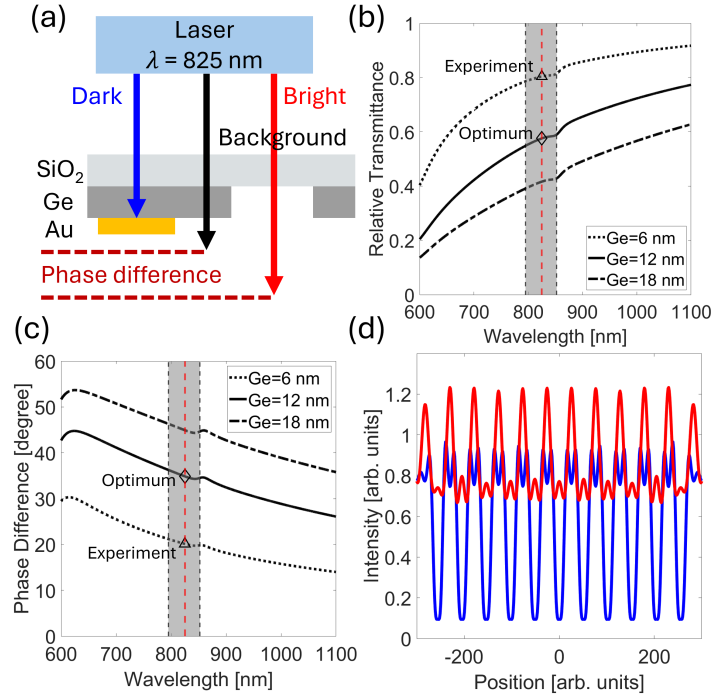


Figure 3: Design of the mask transmittance and phase. **(a)** The mask has three levels of transmittance: (1) The dark traps are produced by circular regions coated with optically thick (opaque) gold; (2) the bright traps are produced by circular open apertures, which are just the bare AR-coated substrate; and (3) the background regions has an intermediate transmittance level, here generated by a 6-nm-thick layer of evaporated amorphous germanium (a-Ge). The high absorption coefficient of a-Ge ensures a small phase difference between the background and the bright region. **(b)** The simulated relative transmittance between the background and the bright regions for a-Ge thicknesses of 6 nm, 12 nm, and 18 nm. **(c)** The simulated phase difference between the background and the bright regions. In both (b) and (c), at wavelength = 825 nm, the triangle marks the phase difference of the experimentally demonstrated design and the diamond marks the optimal design. **(d)** The simulated intensity profiles of both dark (blue) and bright (red) traps at $\lambda_0 = 825$ nm when taking the phase difference into account for the optimum case. Compared to the optimal line profile in Fig. 1(d), both the dark and bright traps are slightly shallower.

a phase difference of 20° compared to the transparent region [Fig. 3(b, c)]. This phase difference is small but not zero, and introduces a more complicated interference pattern in the image plane compared to the case of no phase difference, which leads to shallower trapping depths for both dark and bright traps. A simulated cross-sectional intensity profile accounting for the phase difference is shown in Fig. 3(d).

The sizes of the dark and bright traps at the back focal plane of lens 2 can be controlled by the focal length ratio between the first lens f_1 and the second lens f_2 . Thus, the bright and dark aperture sizes on the intensity mask can be many times larger than the trap sizes, which are usually micron-scale. We chose the radii of the bright disks to be $120 \mu\text{m}$ and dark disks to be $75 \mu\text{m}$ (Table 1), which is trivially achieved with contact photolithography or direct laser writing.

a_{bright}	a_{dark}	Period	Ge thickness
$120 \mu\text{m}$	$75 \mu\text{m}$	$516 \mu\text{m}$	6 nm

Table 1: Physical parameters of fabricated mask.

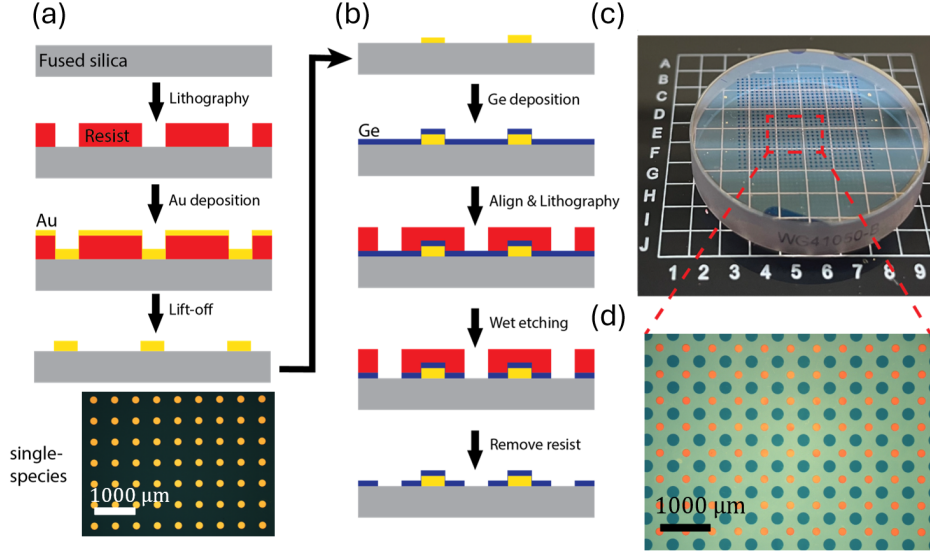


Figure 4: The fabrication processes of the two-species optical mask. **(a)** The dark regions made of 100 nm gold thin films are fabricated by laser lithography, electron-beam evaporation, and lift-off. **(b)** The background regions, comprising 6 nm Ge, are formed by Ge evaporation, lithography with alignment, and etching of Ge. **(c)** The two-species optical mask on a one-inch glass substrate with double-side anti-reflection coating. **(d)** Microscope image of the mask. The distance between adjacent dark disks is $512 \mu\text{m}$, the radius of the bright disks is $120 \mu\text{m}$ and the radius of the dark disks is $75 \mu\text{m}$.

4 Fabrication and characterization

The fabrication process can be separated into two broad steps: the first, presented in Fig. 4(a), results in a mask that can be used for single-species trapping, and then the second step, presented in Fig. 4(b), results in the mask for a two-species trap array.

First, we fabricate the gold disks for dark trapping using a lift-off photolithography process with S1813 resist. After resist development, we evaporate 2 nm of Ti and 100 nm of Au, and perform lift-off. Then, we evaporate the amorphous Ge thin film, resulting in the background region (Fig. 4(b)). Note that the Ge is also deposited on top of the gold regions, but this does not change the transmittance, which is already zero. Then we spin another layer of photoresist, and use laser lithography with alignment to expose the regions that will become the bright traps. The pattern of bright traps is aligned to be in between dark traps with spacing determined by the needs of an atomic experiment or device. After exposure and development, the Ge is etched away using a hydrogen peroxide wet etching process [21], followed by removal of the remaining resist.

Fig. 4(c, d) is a photo and a microscope image of the fabricated two-species mask on a one-inch

AR-coated window. The transmittance of the background region was measured over 4 months in standard lab atmosphere to make sure that it does not change due to oxidation of Ge [22].

5 Trapping Rb and Cs atoms

In our experiment, the mask was illuminated with an 825 nm diode laser amplified by a tapered amplifier (MOGLabs). The incident beam was diffracted using an acousto-optic modulator for intensity control and switching, and then coupled into a single-mode optical fiber. To produce more uniform traps, we used a diffractive top-hat beam generator to generate a square uniform beam profile. This minimizes the spatial variation of trap depths across the array compared to a Gaussian incident beam. After the intensity mask, the beam was de-magnified by a $4f$ optical system with $f_1 = 250$ mm and $f_2 = 125$ mm and shaped by a variable iris on an x-y translation stage mounted in the Fourier plane. The optical setup is shown in Fig. 5(a). A CCD camera is placed at the focal plane of lens 2 to monitor the shape of the trapping beams before further de-magnification into the vacuum cell. The iris was centered on the beam by closing it all the way and optimizing the x-y symmetry of the resulting pattern. Then the iris was opened and adjusted while monitoring the image to maximize the brightness of the bright traps. Fig. 5(b) shows an image of the trap array on the CCD camera. Fig. 5(c) shows the Gaussian-like line profiles of the dark and bright traps highlighted in Fig. 5(b) near the center of the array. Due to higher-than-ideal transmittance in the background region, the trap depths of the dark traps are deeper than the bright traps, but this can be addressed by adjusting the background transmittance level.

After the intermediate-step imaging, a mirror was inserted in the beam path, then a sequence of lenses with focal lengths $f_{3-6} = (200, -50, 250, 23.2)$ mm was used to relay the transmitted light into the vacuum cell for atom trapping (shown in Fig. 6(a)). The 23.2 mm lens is a custom objective lens with high numerical aperture (NA) and correction for the vacuum cell wall, suitable for creating a diffraction-limited image of the trap array at the center of a glass vacuum cell where ^{87}Rb and ^{133}Cs were collected in a dual-species 3D magneto-optical trap (MOT). The de-magnification from the mask to the atoms was $86.2\times$, corresponding to a periodicity of $5.94 \mu\text{m}$ with a total power of 450 mW. Considering the input laser power is approximately 650 mW, the power efficiency of this specific imaging system is about 69%.

Atoms were first loaded into a dual-species MOT. The magnetic quadrupole gradient was abruptly turned off and the detuning of the cooling light from resonance was increased to further cool the atoms via polarization gradient cooling (PGC) [23]. During the PGC phase, atoms were stochastically loaded into the optical tweezer (bright) and bottle (dark) traps, where they underwent collisional blockade [24] until at most one atom per trap site survived. The resulting atom arrays were then imaged by pulsing quasi-resonant light from the side of the vacuum cell (shown in Fig. 6(a)) to induce fluorescence at wavelengths 780 nm for Rb and 852 nm for Cs. This fluorescence was collected via a second high-NA objective on the other side of the vacuum cell. A series of dichroic beamsplitters was used to separate

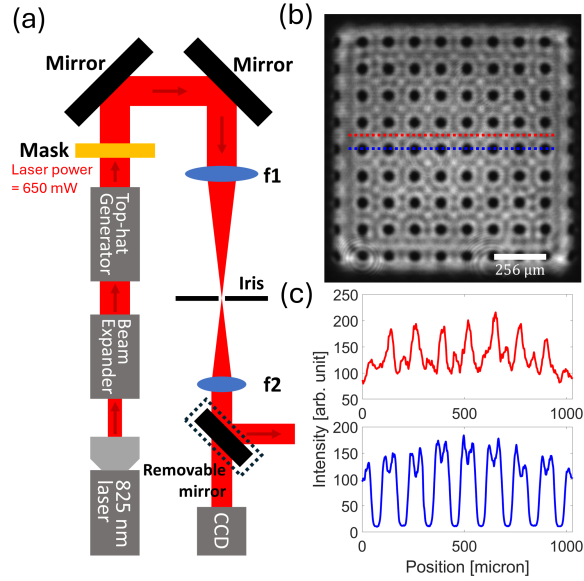


Figure 5: Optical setup. (a) The 825 nm laser is beam-expanded to fill the region on the optical mask that generates the traps shown in (b). To achieve more uniform traps, a diffractive top-hat beam generator is used to produce a square uniform beam profile. The laser power before the mask is approximately 650 mW. The output of the mask is imaged by a CCD camera after $4\times$ de-magnification, while also passing through the spatial filter (iris). A removable mirror is used to image a plane conjugate to the trap in the vacuum cell, as shown in Fig. 5. (b, c) The measured (b) two-dimensional and (c) line profiles of the intensity at the CCD camera.

the trapping light from the fluorescence and to split the fluorescence light into two separate imaging paths, one for each species, before recombining the images of the two interleaved arrays onto a single electron-multiplying charge-coupled device (EMCCD, NuVu HNü512). The imaging separation of Rb and Cs atoms helps increase the signal to background of each species. The averaged fluorescence image of 5000 loading shots collected by the EMCCD is shown in Fig. 6 (a) with the Rb array of atoms in the lower-left and the Cs array in the upper-right. Each atom-trapping site is spatially separated by about $6\ \mu\text{m}$.

In Fig. 6 (b), we reconstructed the atomic fluorescence images of Cs and Rb by aligning the centers of each array. As per the design, the two arrays of different species are interleaved. This image is reconstructed by defining the intensity values of Cs as positive and the intensity values of Rb as negative, then summing them. Cs atoms are shown as yellow [RGB = (1, 1, 0)], and Rb atoms are shown as blue [RGB = (0, 0, 1)]. The line profiles of the fluorescence from Cs and Rb atoms are shown in Fig. 6 (c). In Fig. 6 (d), the atomic fluorescence histograms of Cs and Rb at selected sites are plotted. In each histogram, the left peak is from background noise and the right peak indicates single atom occupation of the trap.

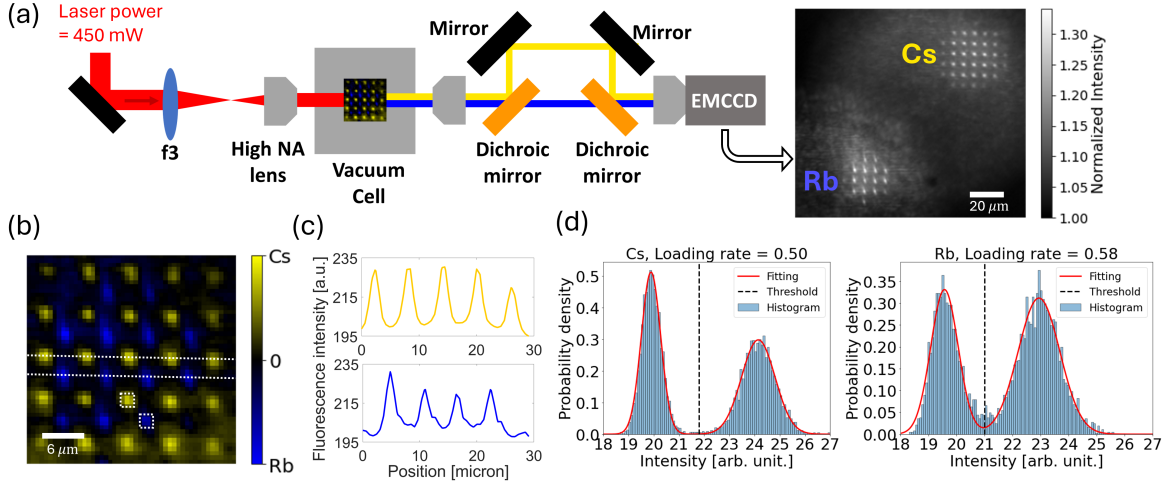


Figure 6: Two-species atom trapping. **(a)** The laser power after the mask and the Fourier filtering is 450 mW. After f_3 and the high-NA lens, the plane in Fig. 5(b) is re-imaged into the vacuum cell with further demagnification, to form the atom traps. On the other side of the vacuum cell, the fluorescence from Rb and Cs atoms is spatially separated to form two fluorescence images on a single EMCCD. The Rb array is imaged at the lower left, and the Cs array is at the upper right of the EMCCD. **(b)** The reconstructed averaged images of the Cs and Rb single-atom arrays, with fluorescence from Cs in yellow and Rb in blue. **(c)** The intensity profiles of the Rb and Cs fluorescence at the specific lines highlighted in (b). **(d)** Histograms of the EMCCD photoelectron counts from individual Cs and Rb sites over 5000 loading shots. The individual Cs and Rb sites are highlighted in (c). The two peaks correspond to the measured intensity from sites with zero atoms, and sites with one atom.

6 Conclusion

We demonstrated simultaneous trapping of individual Rb and Cs atoms, positioned in an atom-specific interleaved grid, using a single trapping laser and an optical system comprising a three-transmittance-level optical mask and a spatial filter. This is a simpler approach to trapping arrays of multiple atomic species compared to the use of active optical components like SLMs, AODs, and DMDs, and multiple lasers. The array generator works for a relatively wide range of wavelengths and is robust to fabrication imperfections. The approach can be readily adapted to any desired configuration of atom traps at any wavelength, and will therefore be useful for a variety of single-atom experiments and applications.

Even though atom loading is stochastic across the array, the simultaneous use of dark and bright traps has the useful feature that Rb atoms are only collected in bright traps and Cs atoms are only collected in dark traps. This reduces the complexity of atom rearrangement for preparing fully occupied, interleaved arrays. Although the use of fabricated components reduces operational complexity compared to active pattern forming devices, such components do not easily allow for correction of optical imperfections that may lead to trap depth variation across the array. Minimization of such variations is important for applications such as optical tweezer clocks[25, 26]. Development of hybrid systems that rely on passive components for the major part of beam shaping while incorporating the ability to make smaller adjustments for improved array uniformity is an interesting direction for future work.

7 Data availability statement

Data underlying the results is openly available in Zenodo at doi.org/10.5281/zenodo.14533096.

8 Acknowledgments

This material is based upon work supported by the U.S. Department of Energy Office of Science National Quantum Information Science Research Centers as well as support from NSF Award 2016136 for the QLCI center Hybrid Quantum Architectures and Networks, and NSF award 2210437.

References

- [1] A. M. Kaufman and K.-K. Ni. Quantum science with optical tweezer arrays of ultracold atoms and molecules. *Nat. Phys.*, 17:1324, 2021.
- [2] TM Graham, Y Song, J Scott, C Poole, L Phuttitarn, K Jooya, P Eichler, X Jiang, A Marra, B Grinkemeyer, et al. Multi-qubit entanglement and algorithms on a neutral-atom quantum computer. *Nature*, 604(7906):457–462, 2022.
- [3] Donggyu Kim, Alexander Keesling, Ahmed Omran, Harry Levine, Hannes Bernien, Markus Greiner, Mikhail D Lukin, and Dirk R Englund. Large-scale uniform optical focus array generation with a phase spatial light modulator. *Optics letters*, 44(12):3178–3181, 2019.
- [4] Hannah J. Manetsch, Gyohei Nomura, Elie Bataille, Kon H. Leung, Xudong Lv, and Manuel Endres. A tweezer array with 6100 highly coherent atomic qubits. *arXiv:2403.12021*, 2024.
- [5] D. Stuart and A. Kuhn. Single-atom trapping and transport in DMD-controlled optical tweezers. *New J. Phys.*, 20:023013, 2018.
- [6] Yibo Wang, Sayali Shevate, Tobias Martin Wintermantel, Manuel Morgado, Graham Lochead, and Shannon Whitlock. Preparation of hundreds of microscopic atomic ensembles in optical tweezer arrays. *npj Quantum Information*, 6(1):54, 2020.
- [7] I. I. Beterov and M. Saffman. Rydberg blockade, Förster resonances, and quantum state measurements with different atomic species. *Phys. Rev. A*, 92:042710, 2015.
- [8] K. Singh, S. Anand, A. Pocklington, J. T. Kemp, and H. Bernien. Dual-element, two-dimensional atom array with continuous-mode operation. *Phys. Rev. X*, 12:011040, 2022.
- [9] K. Singh, C. E. Bradley, S. Anand, V. Ramesh, R. White, and H. Bernien. Mid-circuit correction of correlated phase errors using an array of spectator qubits. *Science*, 380:1265, 2023.

- [10] D. Petrosyan, S. Norrell, C. Poole, and M. Saffman. Fast measurements and multiqubit gates in dual-species atomic arrays. *Phys. Rev. A*, 110:042404, 2024.
- [11] P. Huft, Y. Song, T. M. Graham, K. Jooya, S. Deshpande, C. Fang, M. Kats, and M. Saffman. Simple, passive design for large optical trap arrays for single atoms. *Phys. Rev. A*, 105:063111, 2022.
- [12] Malte Schlosser, Sascha Tichelmann, Dominik Schöffner, Daniel Ohl de Mello, Moritz Hambach, Jan Schütz, and Gerhard Birkel. Scalable multilayer architecture of assembled single-atom qubit arrays in a three-dimensional Talbot tweezer lattice. *Phys. Rev. Lett.*, 130:180601, 2023.
- [13] Ruiting Huang, Feng Zhou, Xiao Li, Peng Xu, Yi Wang, and Mingsheng Zhan. Metasurface optical trap array for single atoms. *Opt. Expr.*, 32:21293–21303, 2024.
- [14] Xiaoyan Huang, Weijun Yuan, Aaron Holman, Minh Kwon, Stuart J Masson, Ricardo Gutierrez-Jauregui, Ana Asenjo-Garcia, Sebastian Will, and Nanfang Yu. Metasurface holographic optical traps for ultracold atoms. *Progress in Quantum Electronics*, 89:100470, 2023.
- [15] Aaron Holman, Yuan Xu, Ximo Sun, Jiahao Wu, Mingxuan Wang, Bojeong Seo, Nanfang Yu, and Sebastian Will. Trapping of single atoms in metasurface optical tweezer arrays. *arXiv preprint arXiv:2411.05321*, 2024.
- [16] M. Saffman, T. G. Walker, and K. Mølmer. Quantum information with Rydberg atoms. *Rev. Mod. Phys.*, 82:2313–2363, 2010.
- [17] P. Scholl, M. Schuler, H. J. Williams, A. A. Eberharter, D. Barredo, K.-N. Schymik, V. Lienhard, L.-P. Henry, T. C. Lang, T. Lahaye, A. M. Läuchli, and A. Browaeys. Quantum simulation of 2D antiferromagnets with hundreds of Rydberg atoms. *Nature*, 595:233–238, 2021.
- [18] G. Semeghini, H. Levine, A. Keesling, S. Ebadi, T. T. Wang, D. Bluvstein, R. Verresen, H. Pichler, M. Kalinowski, R. Samajdar, A. Omran, S. Sachdev, A. Vishwanath, M. Greiner, V. Vuletić, and M. D. Lukin. Probing topological spin liquids on a programmable quantum simulator. *Science*, 374:1242–1247, 2021.
- [19] Matt. J. Bedalov, Matt Blakely, Peter. D. Buttler, Caitlin Carnahan, Frederic T. Chong, Woo Chang Chung, Dan C. Cole, Palash Goiporia, Pranav Gokhale, Bettina Heim, Garrett T. Hickman, Eric B. Jones, Ryan A. Jones, Pradnya Khalate, Jin-Sung Kim, Kevin W. Kuper, Martin T. Lichtman, Stephanie Lee, David Mason, Nathan A. Neff-Mallon, Thomas W. Noel, Victory Omole, Alexander G. Radnaev, Rich Rines, Mark Saffman, Efrat Shabtai, Mariesa H. Teo, Bharath Thotakura, Teague Tomesh, and Angela K. Tucker. Fault-tolerant operation and materials science with neutral atom logical qubits. *arXiv:2412.07670*, 2024.

- [20] Arkadiusz Ciesielski, Lukasz Skowronski, Wojciech Pacuski, and Tomasz Szoplik. Permittivity of Ge, Te and Se thin films in the 200–1500 nm spectral range. predicting the segregation effects in silver. *Materials Science in Semiconductor Processing*, 81:64–67, 2018.
- [21] Inge M Huygens, WP Gomes, and K Strubbe. Etching of germanium in hydrogenperoxide solutions. *ECS Transactions*, 6(2):375, 2007.
- [22] JR Ligenza. The initial stages of oxidation of germanium. *The Journal of Physical Chemistry*, 64(8):1017–1022, 1960.
- [23] J. Dalibard and C. Cohen-Tannoudji. Laser cooling below the Doppler limit by polarization gradients: simple theoretical models. *J. Opt. Soc. Am. B*, 6:2023, 1989.
- [24] Nicolas Schlosser, Georges Reymond, and Philippe Grangier. Collisional blockade in microscopic optical dipole traps. *Physical review letters*, 89(2):023005, 2002.
- [25] Ivaylo S. Madjarov, Alexandre Cooper, Adam L. Shaw, Jacob P. Covey, Vladimir Schkolnik, Tai Hyun Yoon, Jason R. Williams, and Manuel Endres. An atomic-array optical clock with single-atom readout. *Phys. Rev. X*, 9:041052, 2019.
- [26] Aaron W. Young, William J. Eckner, William R. Milner, Dhruv Kedar, Matthew A. Norcia, Eric Oelker, Nathan Schine, Jun Ye, and Adam M. Kaufman. Half-minute-scale atomic coherence and high relative stability in a tweezer clock. *Nature*, 588:408–413, 2020.